

Supplementary Information

Two-Dimensional Nanostructures of Non-Layered Ternary Thiospinels and Their Bifunctional Electrocatalytic Properties for Oxygen Reduction and Evolution: the Case of CuCo_2S_4 Nanosheets

Shulin Zhao,^a Yu Wang,^a Qinghua Zhang,^{b,c} Yafei Li,^a Lin Gu,^b Zhihui Dai,^a Suli Liu,^a Ya-Qian Lan,^a Min Han,^{a,*} and Jianchun Bao^{a,*}

^a Jiangsu Key Laboratory of Biofunctional Materials, School of Chemistry and Materials Science, Nanjing Normal University, Nanjing 210023, P. R. China

^b Beijing National Laboratory for Condensed Matter Physics, Institute of Physics, Chinese Academy of Sciences, Beijing 100190, P. R. China

^c Department of Materials Science and Engineering, Tsinghua University, Beijing 100084, P.R. China

* To whom correspondence should be addressed.

E-mail: 07203@njnu.edu.cn (Prof. Dr. M. Han);

baojianchun@njnu.edu.cn (Prof. Dr. J. C. Bao).

Tel/Fax: +86-25-85891051

This information contains:

- (1) EDS pattern for CuCo_2S_4 NSs (**Fig. S1**)
- (2) AFM image and height profile patterns for CuCo_2S_4 NSs (**Fig. S2**)
- (3) Characterization of the samples obtained by using other metal precursors (**Fig. S3**)
- (4) Characterization of the samples obtained by using other sulfur sources (**Fig. S4**)
- (5) Characterization of binary metal sulphides control catalysts (**Fig. S5**)
- (6) Tafel plots of CuCo_2S_4 NSs and other control catalysts toward ORR (**Fig. S6**)
- (7) Characterization of CuCo_2S_4 NSs catalyst after cycling tests toward ORR (**Fig. S7**)
- (8) Characterization of CuCo_2S_4 NSs catalyst after cycling tests toward OER (**Fig. S8**)
- (9) Comparing bifunctional catalytic activity of CuCo_2S_4 NSs and binary metal sulfides nanostructures (**Fig. S9**)
- (10) Comparing bifunctional catalytic activity of CuCo_2S_4 NSs and other reported bifunctional oxygen electrocatalysts (**Table S1**)
- (11) Comparing bifunctional catalytic activity of the typical CuCo_2S_4 NSs and other CuCo_2S_4 nanostructures (**Fig. S10 and Table S2**)
- (12) The details for theoretical computations (**Table S3 and Fig. S11**)

1. EDS pattern for CuCo_2S_4 NSs

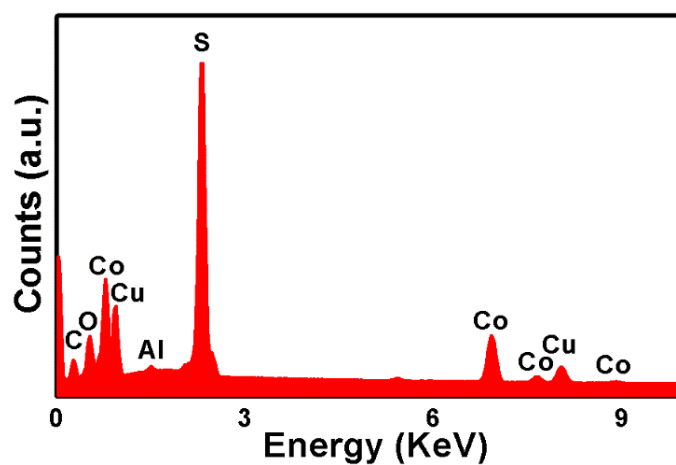


Fig. S1 The EDS pattern of the as-synthesized CuCo_2S_4 NSs.

2. AFM image and height profile patterns for CuCo_2S_4 NSs

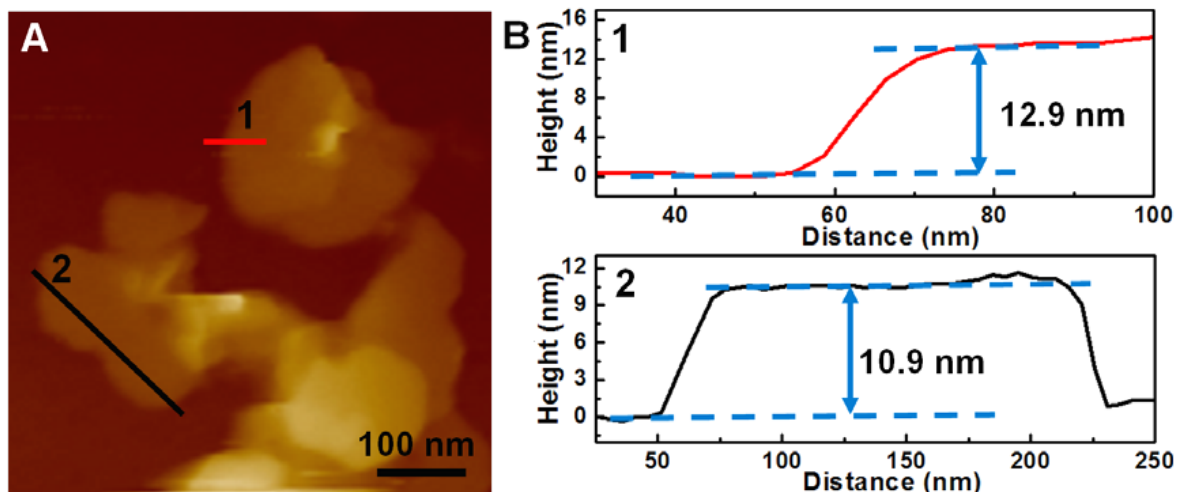


Fig. S2 (A) AFM image for CuCo_2S_4 NSs. (B) The corresponding height profile patterns for the red and black lines indicated areas in (A), respectively.

3. Characterization of the samples obtained by using other metal precursors

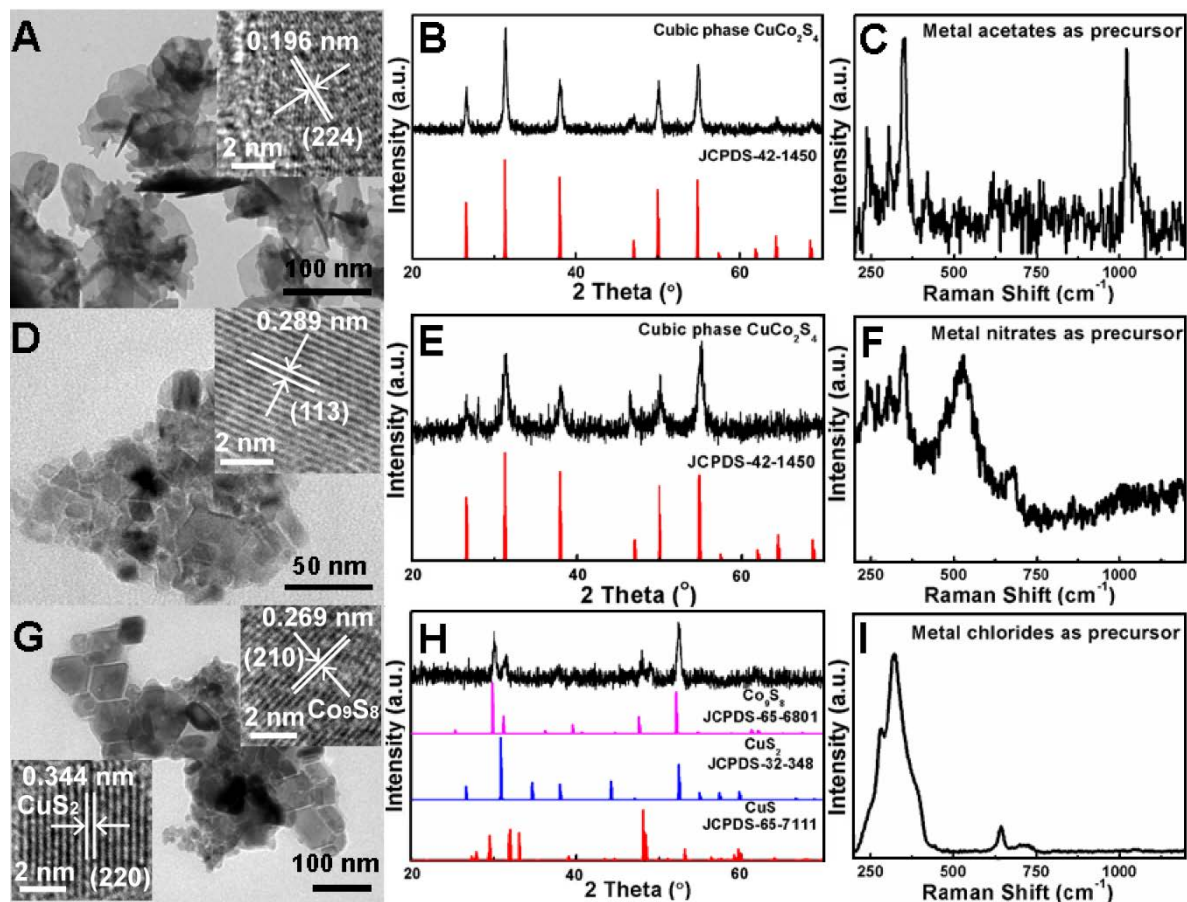


Fig. S3. (A-C) TEM image (inset: HRTEM), XRD pattern and Raman spectrum of the sample obtained by using metal acetates to replace acetylactonate complexes while keeping other conditions constant. (D-F) TEM image (inset: HRTEM), XRD pattern and Raman spectrum of the sample obtained by using metal nitrates to replace acetylactonate complexes while keeping other conditions constant. (G-I) TEM image (inset: HRTEM), XRD pattern and Raman spectrum of the sample obtained by using metal chlorides to replace acetylactonate complexes while keeping other conditions constant.

4. Characterization of the samples obtained by using other sulfur sources

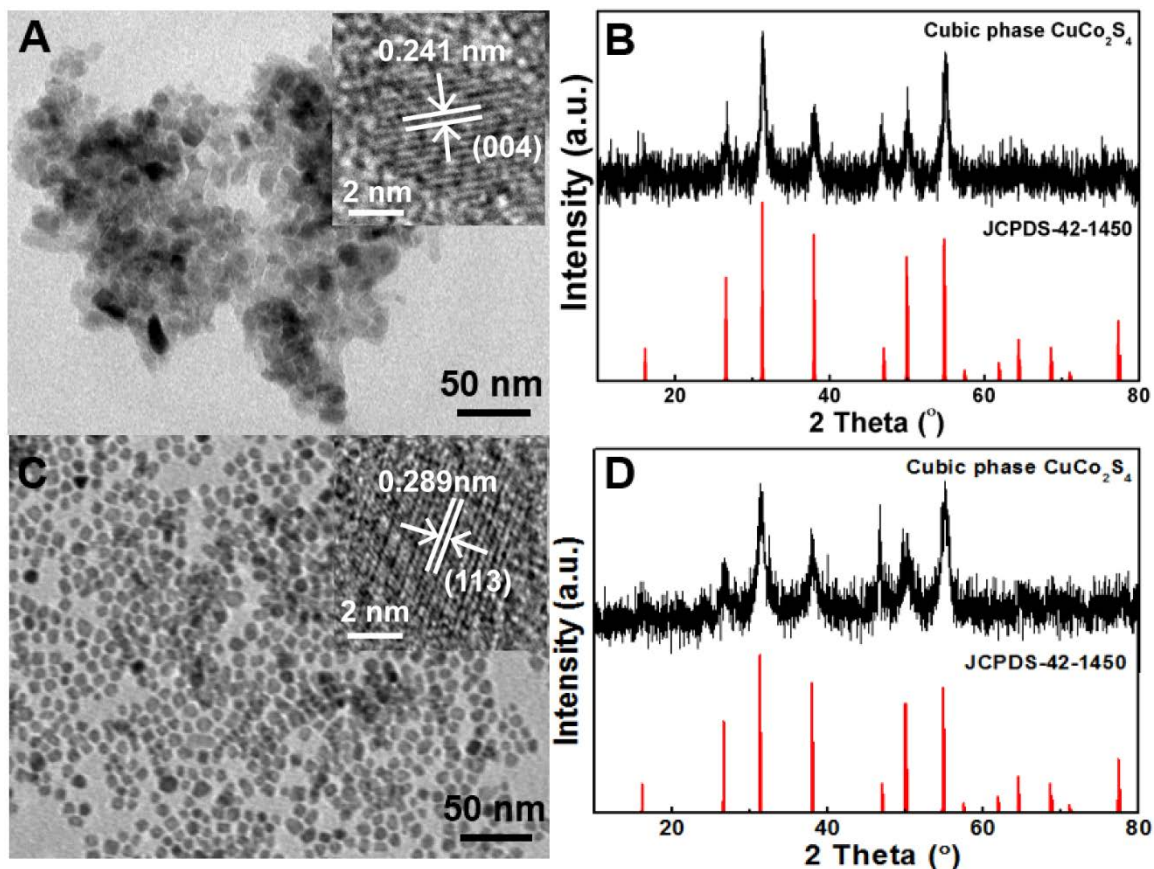


Fig. S4 (A, B) TEM image (inset: HRTEM) and XRD pattern of the sample obtained by using sulfur powder to replace DDT and keeping other conditions unchanged. (C, D) TEM image (inset: HRTEM) and XRD pattern of the sample obtained by using thioacetamide to replace DDT and keeping other conditions constant.

5. Characterization of binary metal sulphides control catalysts

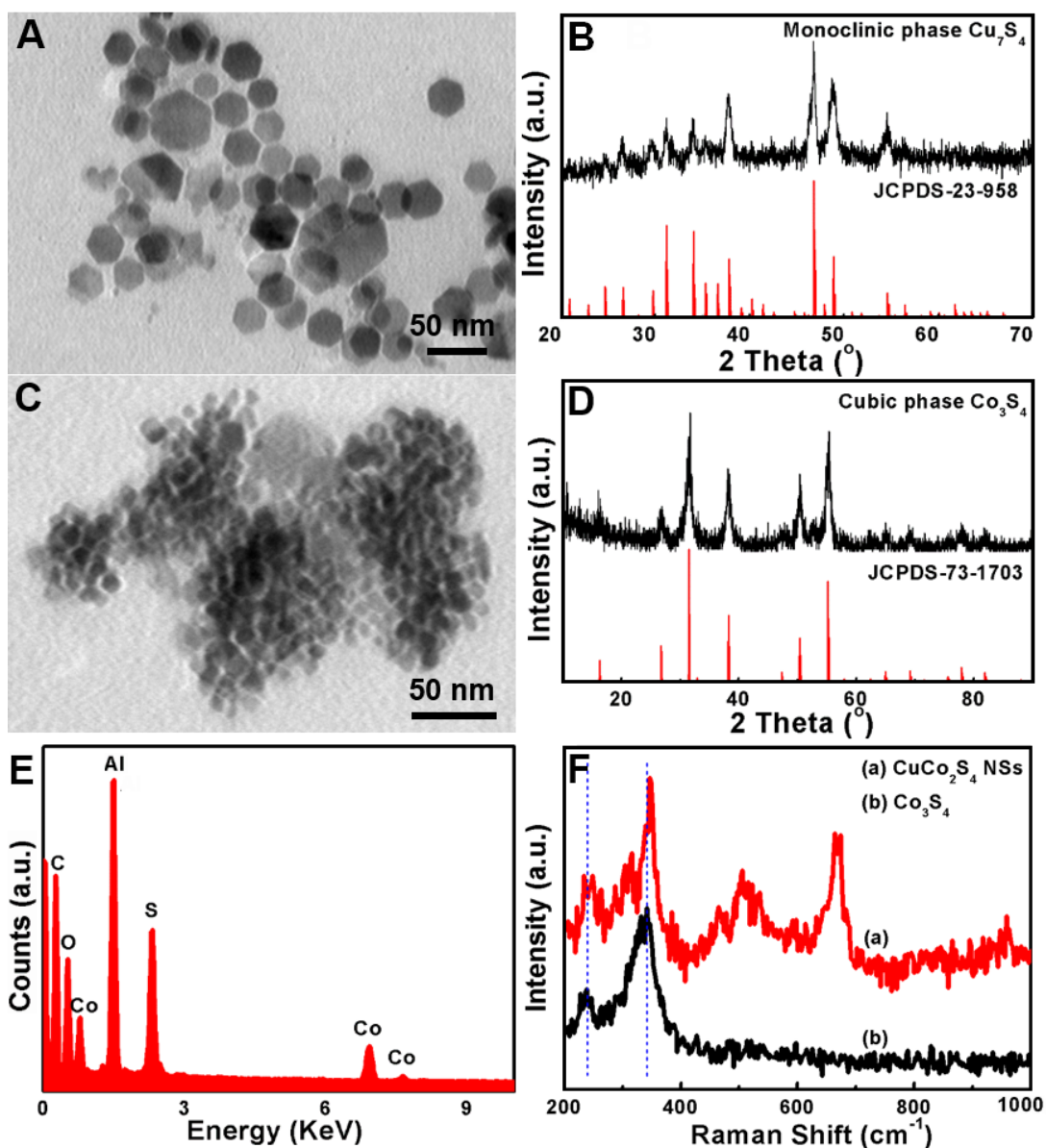


Fig. S5 (A, B) TEM image and XRD pattern of the Cu_7S_4 nanodisks. (C, D) TEM image and XRD pattern of the Co_3S_4 nanocrystals. (E, F) EDS pattern and Raman spectrum of Co_3S_4 nanocrystals. It should be mentioned that the XRD pattern of Co_3S_4 nanocrystals is similar to that of CuCo_2S_4 NSs. To distinguish them, the EDS pattern of Co_3S_4 nanocrystals is given in (E), which is obtained by dispersing the sample on high-purity Al sheet. In addition, the Raman spectral of Co_3S_4 nanocrystals and CuCo_2S_4 NSs are placed together in (F) with the aim to highlight their differences. The peaks between $200\text{-}400\text{ cm}^{-1}$ originate from the vibration of Co-S bond (*Angew. Chem. Int. Ed.* 2015, **54**, 11231) and the peaks between $400\text{-}1200\text{ cm}^{-1}$ are attributed to the vibration of Cu-S bond.

6. Tafel plots of CuCo_2S_4 NSs and other control catalysts toward ORR

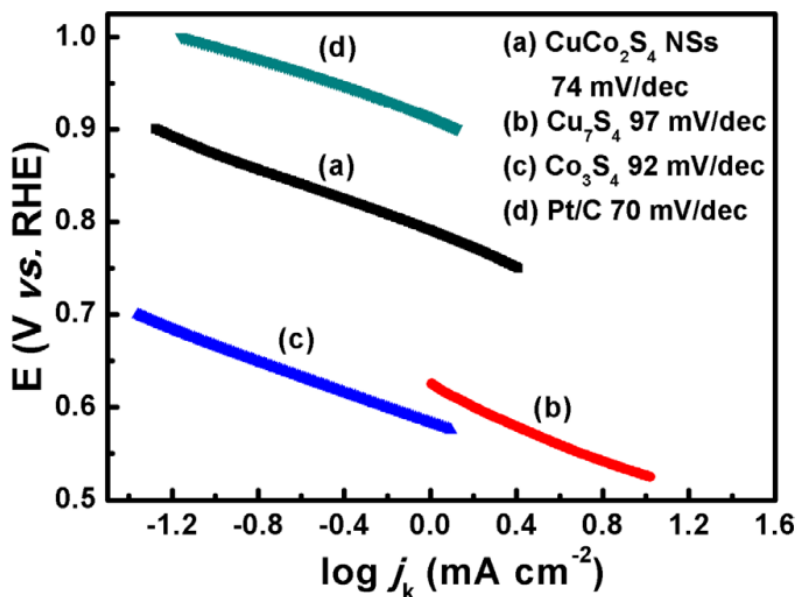


Fig. S6 The Tafel plots of CuCo_2S_4 NSs (a), Cu_7S_4 nanodisks (b), Co_3S_4 nanocrystals (c), and commercial Pt/C (d) catalysts toward ORR, respectively.

7. Characterization of CuCo_2S_4 NSs catalyst after cycling tests toward ORR

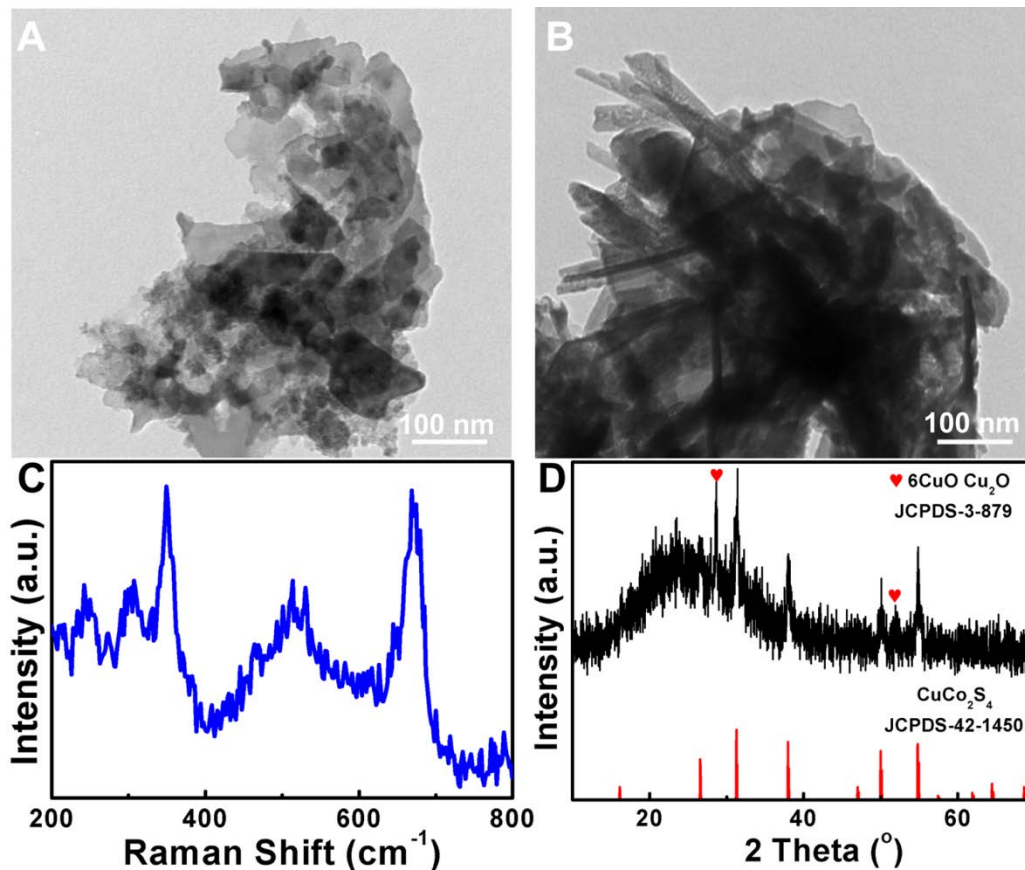


Fig. S7 A-B) TEM images of the CuCo_2S_4 NSs catalyst after cycling tests toward ORR. C-D) Corresponding Raman spectrum (C) and XRD pattern (D) for the CuCo_2S_4 NSs catalyst after cycling tests toward ORR.

To tentatively understand the origin of ORR activity loss, the samples after ORR cycling tests have been collected by repeating the cycling tests for many times, whose structure and composition are characterized by TEM, Raman and XRD. The related TEM images, Raman spectrum and XRD pattern are shown in Fig. S7. The TEM analysis (Fig. S7A-B) reveals that there is a relatively large change on the morphology of the samples after cycling tests. The original large CuCo_2S_4 NSs are frustrated and broken apart into small fragments or debris, which are restacked and aggregated into larger particles. Additionally, a certain amount of cavities or pores can be observed from some debris (Fig. S7B). Corresponding Raman spectrum (Fig. S7C) and XRD analysis (Fig. S7D) demonstrate that the main component of the samples after ORR cycling tests is still CuCo_2S_4 (JCPDS-42-1450). But a small amount of Cu oxide species (JCPDS-3-879) may be formed on their surfaces, as evidenced from the related XRD pattern (Fig. S7D). That is to say, the samples after ORR cycling tests are only slightly oxidized to generate a small amount of Cu oxide species (JCPDS-3-879) on their surfaces, unlike the samples after OER cycling tests. Based on the above analysis, we conjecture that the ORR activity loss of CuCo_2S_4 NSs may be attributed to the large morphology variation or frustration along with the slight oxidation to form small amount of Cu oxide species on their surfaces under long-term electrochemical cycling, which may reduce electronic conductivity of the catalyst and decrease the available active sites or crystal planes for ORR.

8. Characterization of CuCo_2S_4 NSs catalyst after cycling tests toward OER

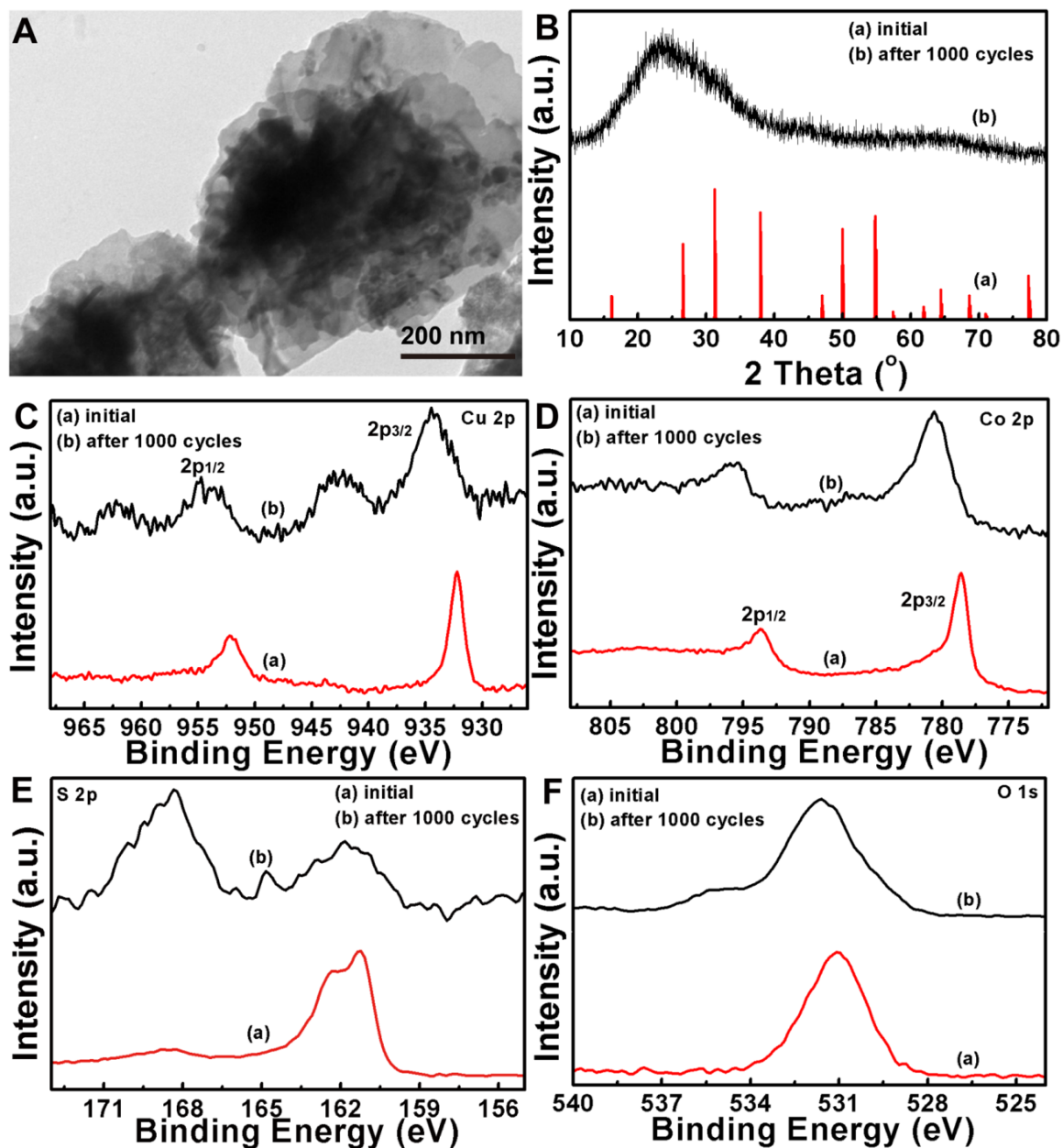


Fig. S8 A-B) TEM image (A) and XRD pattern (B) of the CuCo_2S_4 NSs catalyst after cycling tests toward OER. C-F) Corresponding Cu 2p (C), Co 2p (D), S 2p (E), and O 1s (F) fine XPS spectra for the CuCo_2S_4 NSs catalyst after cycling tests toward OER.

To tentatively understand the origin of the instability of our CuCo_2S_4 NSs for OER, the enough samples after cycling tests are collected by repeating the cycling tests for many times,

whose structure and composition are characterized by TEM, XRD and XPS. The related TEM image, XRD and XPS patterns are shown in Fig. S8. From the TEM image (Fig. S8A), we can see that the sheet-like appearance of the initial CuCo_2S_4 NSs are reserved, but those NSs trend to fracture and re-stack or agglomerate, which may lead to decrease the available active surfaces and reduce the OER activity. The corresponding XRD pattern (Fig. S8B) only exhibits a large and broad peak, indicating that the initial crystallized CuCo_2S_4 NSs become amorphous after cycling tests. To further identify the component of the sample after cycling tests, XPS spectra are also carried out. Compared with that of initial CuCo_2S_4 NSs catalyst, the fine Cu $2p_{3/2}$ (934.4 eV) and $2p_{1/2}$ (953.9 eV) of the sample after cycling tests are shifted to high binding energies (BEs) direction (Fig. S8C). Additionally, two characteristic shakeup satellite peaks at the BEs of 942.5 and 962.3 eV that corresponding to Cu (II) ions are also observed, indicating that the surface Cu (I) ions of initial CuCo_2S_4 NSs are oxidized into Cu (II) ions after continuous electrochemical cycling. That is to say, the surface of initial CuCo_2S_4 NSs may be partially or fully oxidized after continuously working for 10 h. Further evidences come from Co 2p and S 2p fine XPS spectra after cycling tests. Similar to Cu 2p fine spectra, the fine Co $2p_{3/2}$ (780.6 eV) and $2p_{1/2}$ (795.5 eV) peaks of the sample after cycling tests are also shifted to high BEs direction (Fig. S8D). In addition, two small characteristic satellite peaks for Co (III) ions are also seen, revealing that the surface Co(II) ions in initial CuCo_2S_4 NSs catalyst may be oxidized into Co(III) ions. As for S 2p spectra (Fig. S8E), except for reserving the features of S 2p peaks in initial CuCo_2S_4 NSs at the BEs ranging from 165-155 eV, another strong and broad peak at the BEs of 172-165 eV region is observed in the sample after cycling tests. In previous reports, this peak is assigned to the oxidation of S element into the $-\text{SO}_3\text{H}$ or $-\text{SO}_4$ forms. Here, this peak can't be simply assigned to the oxidation of S element because the Nafion (containing $-\text{SO}_3\text{H}$ groups) is used to prepare the modified electrode for OER, which may be retained in the sample after cycling tests *via* ultrasonic exfoliation from the electrode surface. To assign exactly and considering the Cu and Co 2p spectra, we consider that this additional peak in S 2p spectra may has two origins. One is from the residual Nafion reagent, and the other is from the surface partial oxidation of S element of initial CuCo_2S_4 NSs during the electrochemical cycling. Further

evidence comes from the O 1s fine spectra (Fig. S8F). Based on TEM, XRD and XPS analysis, we think that our CuCo_2S_4 NSs are partially oxidized during the OER cycling to form amorphous oxides on their surfaces, which may be the origin for reducing the activity of CuCo_2S_4 NSs catalyst. Further work on alleviation or suppressing the surface oxidation and improve the electrocatalytic stability of CuCo_2S_4 NSs for OER is underway in our lab.

9. Comparing bifunctional catalytic activity of CuCo_2S_4 NSs and binary metal sulfides nanostructures

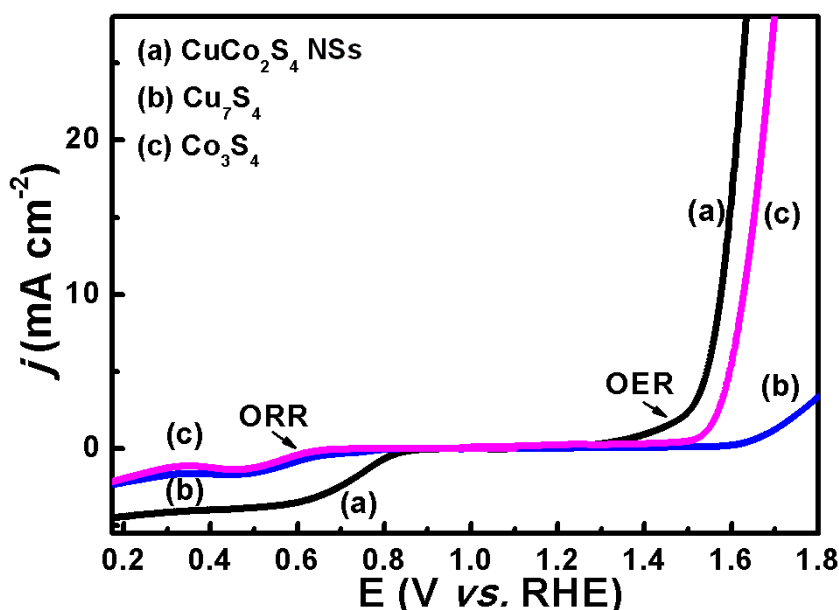


Fig. S9 Comparison of the bifunctional catalytic activity of the typical CuCo_2S_4 NSs (a) with that of Cu_7S_4 nanodisks (b) and Co_3S_4 nanocrystals (c).

10. Comparing bifunctional catalytic activity of CuCo_2S_4 NSs and other reported bifunctional oxygen electrocatalysts

Table S1. Comparison of the bifunctional catalytic activity of CuCo_2S_4 NSs with other reported bifunctional oxygen electrocatalysts

Catalysts	loading (mg cm^{-2})	$E_{1/2}$ (V)	E_{10} (V)	ΔE (V)	Ref.
20% Pt/C	-	0.86	2.02	1.16	(1)
Mn oxide	-	0.73	1.77	1.04	(1)

Mn₂O₃ film	0.14	0.71	1.81	1.81	(2)
α-MnO₂-SF		0.79	1.72	0.93	(3)
α-MnO₂-HT		0.81	1.72	0.91	(3)
Ni/α-MnO₂-SF		0.78	1.74	0.96	(3)
Amorphous MnOx	0.204	0.69	1.82	1.13	(3)
β-MnO₂		0.72	1.83	1.11	(3)
δ-MnO₂		0.68	1.97	1.29	(3)
Co₃O₄/N/BGHSs	-	0.862	1.725	0.863	(4)
Co_xMn_{3-x}O₄		0.72	1.81a	1.09a	(5)
(CoMnO-B)			1.71b	0.99b	
Co_xMn_{3-x}O₄	-	0.77	1.91a	1.14a	(5)
(CoMnO-P)			1.78b	1.01b	
CoMn₂O₄/C	0.051	0.75	1.838	1.088	(6)
MnCo₂O₄/C		0.70	1.748	1.048	(6)
CoFe₂O₄ (crystalline)	0.051	0.65	1.72	1.07	(7)
Amorphous Co-Fe-O		0.75	1.68	0.93	(7)
LiCoO₂		0.56	1.64	1.08	(8)
Li_{0.5}CoO₂		0.68	1.62	0.94	(8)
Li_{0.6}CoO₂	0.25	0.65	1.625	0.975	(8)
Li_{0.8}CoO₂		0.62	1.615	0.995	(8)
Co₃O₄		0.59	1.66	1.07	(8)
Co₃O₄/2.7Co₂MnO₄	0.14	0.71	1.77	1.06	(9)
Ni_{0.4}Co_{2.6}O₄ (2500rpm)	-	0.75	1.74	0.99	(10)
CCH₂/C	0.18	0.84	1.735	0.895	(11)
CoS₂(400)/N,S-GO		0.82	1.61	0.79	(12)
CoS₂(500)/N,S-GO	0.25	0.78	1.62	0.84	(12)
Co₉S₈(600)/N,S-GO		0.78	1.63	0.85	(12)
Co_xS_y@C-1000	0.14	0.824	1.70	0.88	(13)
Co₉S₈/N-C	0.8	0.77	1.58	0.81	(14)
NiCo₂S₄@N-S/rGO	0.283	0.80	1.74	0.94	(15)
Co₃S₄@N-S/rGO		0.80	1.76	0.96	(15)
NiCo₂S₄	0.1	0.6	1.62	1.02	(16)
Co₃S₄		0.55	1.66	1.11	(16)
Co/N-C-800	0.25	0.74	1.599	1.599	(17)
N,P-doped G/C NSs	0.141	0.86	1.57	0.71	(18)
N-Doped G/CNTs	0.255	0.7	1.63	0.93	(19)
Layered Double Oxide/CNT	0.255	0.68	1.64	0.96	(20)
N-doped porous C/CNTs	0.21	0.82	1.56	0.74	(21)
Co NP@NC/NG-700	0.08	0.79	1.62	0.83	(22)
N-doped G mesh	0.255	0.77	1.67	0.90	(23)
CuCo₂S₄ NPs	0.204	0.56	1.72	1.16	this work
CuCo₂S₄ NSs	0.204	0.74	1.575	0.835	this work

[Notes]: All the potential values here are vs. RHE for comparison. The $E_{1/2}$ stands for the half-wave potential for ORR. And E_{10} represents for the potential at the current density of 10 mA cm^{-2} for OER. As for ΔE , it is the potential drop used for evaluating the bifunctional catalytic property of a desired catalyst, which is calculated according to the following formula: $\Delta E = E_{10} - E_{1/2}$. The symbol of “-” means that the related parameters are not given in the literature. In the reported nanocrystalline spinel $\text{Co}_x\text{Mn}_{3-x}\text{O}_4$ (containing tetragonal phase CoMn_2O_4 (CoMNO-B) and cubic phase CoMnO-P) catalysts for ORR and OER,⁽⁵⁾ the diameter of used working electrode is not given in the manuscript, so it is difficult to calculate the E_{10} data. Usually, the diameter of the glassy carbon disk electrode used for ORR and OER tests is 5 mm or 3 mm. For comparison, we use the two kinds of electrode diameters to estimate the E_{10} from the given electrochemical plots in Ref. (5). The symbols of the superscripts “a” and “b” stand for the data obtained by hypothesizing that the diameter of used electrode is 5 mm and 3 mm, respectively.

References

- (1) Y. Gorlin and T. F. Jaramillo, *J. Am. Chem. Soc.*, 2010, **132**, 13612.
- (2) K. L. Pickrahn, S. W. Park, Y. Gorlin, H.-B.-R. Lee, T. F. Jaramillo and S. F. Bent, *Adv. Energy Mater.*, 2012, **2**, 1269.
- (3) Y. Meng, W. Song, H. Huang, Z. Ren, S. Y. Chen and S. L. Suib, *J. Am. Chem. Soc.*, 2014, **136**, 11452.
- (4) Z. Jiang, Z. J. Jiang, T. Maiyalagan and A. Manthiram, *J. Mater. Chem. A*, 2016, **4**, 5877.
- (5) F. Cheng, J. Shen, B. Peng, Y. Pan, Z. Tao and J. Chen, *Nat. Chem.*, 2011, **3**, 79.
- (6) P. W. Menezes, A. Indra, N. R. Sahraie, A. Bergmann, P. Strasser and M. Driess, *ChemSusChem* 2015, **8**, 164.
- (7) A. Indra, P. W. Menezes, N. R. Sahraie, A. Bergmann, C. Das, M. Tallarida, D. Schmeisser, P. Strasser and M. Driess, *J. Am. Chem. Soc.*, 2014, **136**, 17530.
- (8) T. Maiyalagan, K. A. Jarvis, S. Therese, P. J. Ferreira and A. Manthiram, *Nat. Commun.*, 2014, **5**, 3949.
- (9) D. Wang, X. Chen, D. G. Evans and W. Yang, *Nanoscale*, 2013, **5**, 5312.

- (10) T. N. Lambert, J. A. Vigil, S. E. White, D. J. Davis, S. J. Limmer, P. D. Burton, E. N. Coker, T. E. Beechem and M. T. Brumbach, *Chem. Commun.*, 2015, **51**, 9511.
- (11) Y. Wang, W. Ding, S. Chen, Y. Nie, K. Xiong and Z. Wei, *Chem. Commun.*, 2014, **50**, 15529.
- (12) P. Ganesan, M. Prabu, J. Sanetuntikul and S. Shanmugam, *ACS Catal.*, 2015, **5**, 3625.
- (13) B. Chen, R. Li, G. Ma, X. Gou, Y. Zhu and Y. Xia, *Nanoscale*, 2015, **7**, 20674.
- (14) X. Cao, X. Zheng, J. Tian, C. Jin, K. Ke and R. Yang, *Electrochim. Acta*, 2016, **191**, 776.
- (15) Q. Liu, J. Jin and J. Zhang, *ACS Appl. Mater. Interfaces* 2013, **5**, 5002.
- (16) M. Wang, Y. Lai, J. Fang, F. Qin, Z. Zhang, J. Li and K. Zhang, *Catal. Sci. Technol.*, 2016, **6**, 434.
- (17) Y. Su, Y. Zhu, H. Jiang, J. Shen, X. Yang, W. Zou, J. Chen and C. Li, *Nanoscale*, 2014, **6**, 15080.
- (18) R. Li, Z. Wei and X. Gou, *ACS Catal.*, 2015, **5**, 4133.
- (19) G. L. Tian, M. Q. Zhao, D. Yu, X. Y. Kong, J. Q. Huang, Q. Zhang and F. Wei, *Small*, 2014, **10**, 2251.
- (20) H.-F. Wang, C. Tang, X. Zhu and Q. Zhang, *J. Mater. Chem. A*, 2016, **4**, 3379.
- (21) X. Li, Y. Fang, S. Zhao, J. Wu, F. Li, M. Tian, X. Long, J. Jin and J. Ma, *J. Mater. Chem. A*, 2016, **4**, 13133.
- (22) X. Zhong, Y. Jiang, X. Chen, L. Wang, G. Zhuang, X. Li and J. -G. Wang, *J. Mater. Chem. A*, 2016, **4**, 10575.
- (23) C. Tang, H. F. Wang, X. Chen, B. Q. Li, T. Z. Hou, B. Zhang, Q. Zhang, M. M. Titirici and F. Wei, *Adv. Mater.*, 2016, **28**, 6845.

11. Comparing bifunctional catalytic activity of the typical CuCo₂S₄ NSs and other CuCo₂S₄ nanostructures

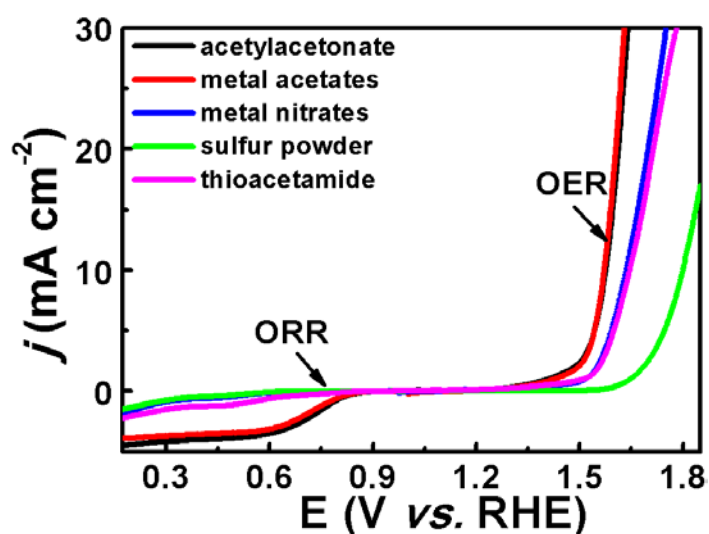


Fig. S10 Comparison of the bifunctional catalytic activity of the typical CuCo_2S_4 NSs (using acetylacetonate complexes as the precursors) with those of CuCo_2S_4 nanostructures obtained from other metal precursors and sulfur resources.

Table S2 Comparison of the bifunctional catalytic activity of the typical CuCo_2S_4 NSs with those of other CuCo_2S_4 nanostructures obtained from other metal precursors and sulfur resources

CuCo_2S_4 catalysts obtained by using distinct precursors	$E_{1/2}$ (V)	$E_{10 \text{ mA cm}^{-2}, \text{OER}}$ (V)	$\Delta E = (E_{10} - E_{1/2})$ (V)
Acetylacetonates	0.74	1.575	0.835
Acetates	0.7	1.572	0.872
Nitrates	0.52	1.636	1.116
Sulfur powder	0.52	1.8	1.28
Thioacetamide	0.56	1.72	1.16

12. The details for theoretical calculations

The spin-polarized density functional theory (DFT) calculations were performed using the plane-wave technique implemented in the Vienna *ab Initio* Simulation package (VASP),^{1,2} with exchange-correlation interactions modeled by the Perdew-Burke-Ernzerhof (PBE) generalized gradient approximation (GGA) function.³ The ion-electron interaction is modeled using the projector-augmented plane wave (PAW) approach.^{4,5} A plane-wave cutoff energy of 360 eV was adopted in all computation. The Brillouin zone was sampled with $3\times 4\times 1$ for (022) planes and $4\times 4\times 1$ k-points for (004) as well as (111) planes. Besides, the electronic structure calculations were employed with a Fermi-level smearing of 0.1 and 0.01 eV for surfaces and gas-phase species calculations, respectively. The convergence threshold was conducted as 10^{-4} eV in energy and 0.02 eV/Å in force, and a vacuum region of around 15 Å was set along the z direction to avoid the interaction between periodic images.

To investigate the ORR/OER performance of CuCo_2S_4 , we first constructed appropriate computational models for CuCo_2S_4 . In this regard, the more energetically favorable and mainly exposed surfaces, namely (004), (111), and (022) planes, were adopted to act as the active surface for the studied system, since the more stable and exposed surfaces play crucial roles in electrocatalysis according to previous studies.⁶⁻¹¹ Briefly, (004) and (022) facets were both modeled with four atomic layers where only the top two layer (plus adsorbates) were allowed to fully relax, whereas (111) facet was constructed with six atomic layers where only the top three layers (plus adsorbates) were allowed to fully relax. According to our calculations, it is found that the most energetically favorable surface is (004) facet, followed by (111) and (022) facets, consistent with previous calculations for the similar system.¹² We also note here that the most stable termination has been chosen for each studied surfaces.

We explore the mechanism underlying the superior catalytic activity based on computational hydrogen electrode (CHE) model.^{错误!未定义书签。} The free energy for each adsorbed and gas-phase species is calculated as:

$$G = E_{DFT} + E_{ZPE} - TS$$

where E_{DFT} is the DFT total energy, E_{ZPE} is the zero point energy, S is the entropy, and T is the system temperature (298.15 K, in our work). E_{ZPE} and S are calculated from the temperature, pressure and calculated vibrational energy by using standard methods. For free energies of adsorbates, all $3N$ degrees of freedom are treated as vibrational motions while neglecting the contributions from the catalysts surfaces. The relevant contributions to the free energy for each gas-phase species and adsorbates are listed in Table S3. Moreover, the free energy of oxygen molecule is calculated using the equation $G(\text{O}_2) = 2G(\text{H}_2\text{O}) - 2G(\text{H}_2) + 4.92$ eV, because the high-spin ground state of O_2 is notoriously poorly described in DFT calculations. The free energy of OH^- is derived as $G(\text{OH}^-) = G(\text{H}_2\text{O}) - G(\text{H}^+)$, and $G(\text{H}^+ + \text{e}^-)$ is taken as $1/2G(\text{H}_2) - eU + \Delta G_{pH}$, where U is the operating electrochemical potential. ΔG_{pH} is calculated using the equation $\Delta G_{pH} = -k_B T \ln 10 \times \text{pH}$ and the value of pH in this work is 13; however, for convenience of reference to Pt(111) and IrO_2 , the free energy diagram shown in this paper has performed potential correction. For example, the zero potential in Figure 6 denotes $U^{\text{RHE}} = 0$ ($U^{\text{NHE}} = -0.77$ V).

Table S3: Contributions to the free energy for gas-phase species and adsorbates from zero-point energy correction (E_{ZPE}), entropy (TS), and the total free energy correction ($G - E_{elec}$).

Species	E_{ZPE} (eV)	$-TS$ (eV)	$G - E_{elec}$ (eV)
H₂	0.27	-0.42	-0.15
H₂O	0.56	-0.67	-0.11
OH*	0.343	-0.108	0.235
O*	0.060	-0.081	-0.021
OOH*	0.438	-0.181	0.257

The Gibbs free energy difference for all ORR/OER steps on the CuCo₂S₄ NSs is defined as:

$$\Delta G = \Delta E_{DFT} + \Delta E_{ZPE} - T\Delta S$$

The reaction energy (ΔE) can be directly determined by analyzing the DFT total energies. Our calculations demonstrate that (022) and (004) planes are in favor of ORR and OER respectively, whereas (111) plane shows poor catalytic performance due to its quite strong adsorption for the adsorbates, as shown in **Fig. S11A-B**. Therefore, in the main text, only (022) and (004) facets are discussed in details to elucidate the superior bifunctional catalytic activity of CuCo₂S₄ NSs. The related free energy profiles for the OER pathway on (022) plane and the ORR pathway on (004) plane are given in **Fig. S11C-D**. On the other hand, according to the method developed by Nørskov *et al.*,^{6,8} the overpotentials for ORR and OER are calculated using the equation:

$$G^{\text{ORR/OER}} = \max\{\Delta G_1, \Delta G_2, \Delta G_3, \Delta G_4\};$$

$$\eta^{\text{ORR}} = (1.23 + G^{\text{ORR}}/e) \text{ V};$$

$$\eta^{\text{OER}} = (G^{\text{OER}}/e - 1.23) \text{ V}.$$

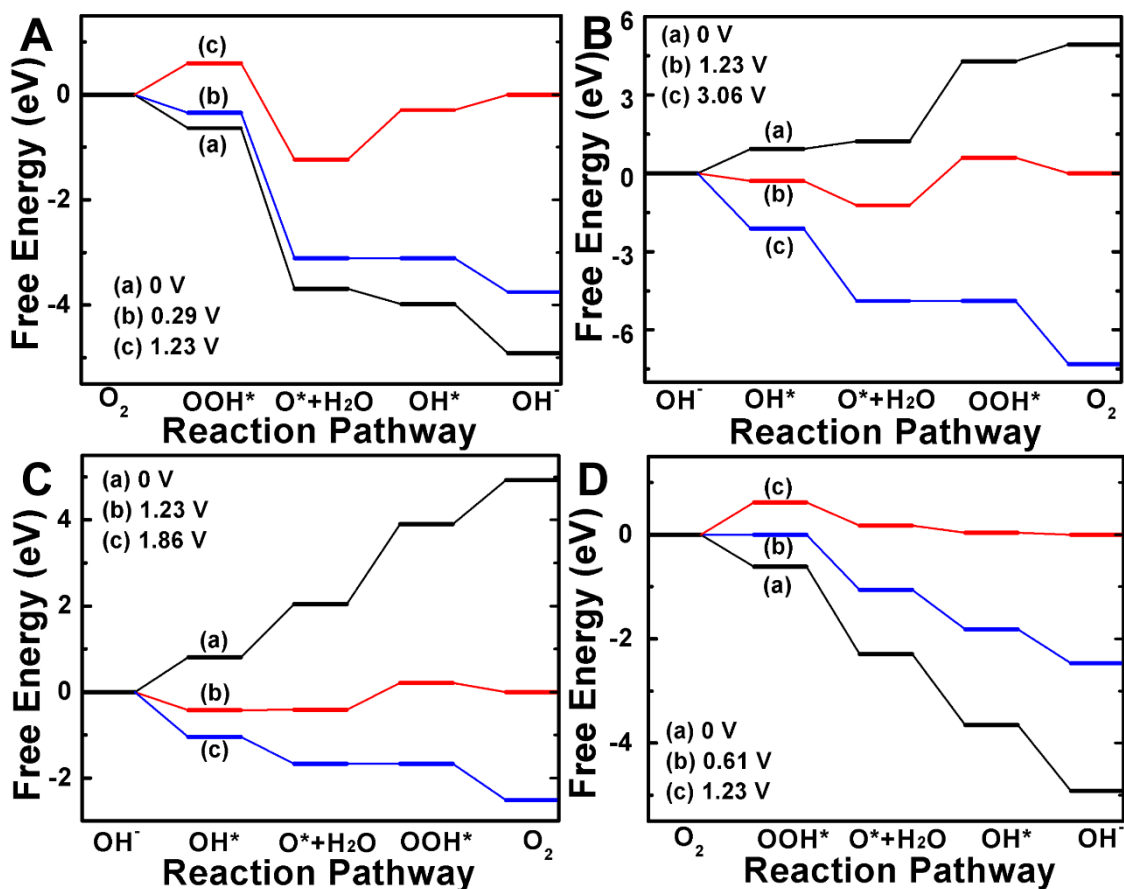


Fig. S11 (A-B) The free energy profile for the ORR pathway on the (111) plane (A) and the OER pathway on (111) plane (B) at different potential. (C-D) The free energy profile for the OER pathway on (022) plane (C), and the ORR pathway on (004) plane (D). The black, red, and blue lines represent the zero potential, the equilibrium potential, and the limiting potential, respectively.

References

- (1) G. Kresse and J. Hafner, *Phys. Rev. B*, 1993, **47**, 558.
- (2) G. Kresse and J. Furthmüller, *Comput. Mater. Sci.*, 1996, **6**, 15.
- (3) J. P. Perdew, K. Burke and M. Ernzerhof, *Phys. Rev. Lett.*, 1996, **77**, 3865.
- (4) P. E. Blöchl, *Phys. Rev. B*, 1994, **50**, 17953.

- (5) G. Kresse and D. Joubert, *Phys. Rev. B*, 1999, **59**, 1758.
- (6) J. K. Nørskov, J. Rossmeisl, A. Logadottir, L. Lindqvist, J. R. Kitchin, T. Bligaard and H. Jónsson, *J. Phys. Chem. B*, 2004, **108**, 17886.
- (7) J. Rossmeisl, A. Logadottir and J. K. Nørskov, *Chem. Phys.*, 2005, **319**, 178.
- (8) I. C. Man, H. -Y. Su, F. Calle-Vallejo, H. A. Hansen, J. I. Martínez, N. G. Inoglu, J. Kitchin, T. F. Jaramillo, J. K. Nørskov and J. Rossmeisl, *ChemCatChem*, 2011, **3**, 1159.
- (9) A. A. Peterson, F. Abild-Pedersen, F. Studt, J. Rossmeisl and J. K. Nørskov, *Energy Environ. Sci.*, 2010, **3**, 1311.
- (10) A. A. Peterson and J. K. Nørskov, *J. Phys. Chem. Lett.*, 2012, **3**, 251.
- (11) J. K. Nørskov, T. Bligaard, A. Logadottir, J. R. Kitchin, J. G. Chen, S. Pandelov and U. Stimming, *J. Electrochem. Soc.*, 2005, **152**, 23.
- (12) S. Haider, A. Roldan and N. H. de Leeuw, *J. Phys. Chem. C*, 2014, **118**, 1958.